AGU
ADVANCING EARTH AND SPACE SCIENCE

Geophysical Research Letters®

Combined Analysis of Hydrogen and Oxygen 102.6 nm Emission at Mars

Key Points:

- We present the first observations of 102.6 nm emission at Mars that reveal the independent contributions of hydrogen and oxygen
- We successfully reproduce the coronal emission with the first model to include the complete O 102.6 nm system
- Reproduction of observed disk O 102.6 nm emission will require incorporating additional physics into the model

Correspondence to:

M. S. Chaffin,
michael.chaffin@colorado.edu

Michael S. Chaffin[1] , **Justin Deighan[1]** , **Sonal Jain[1]** , **Greg Holsclaw[1]** , **Hoor AlMazmi[2]** , **Krishnaprasad Chirakkil[1,3]** , **John Correira[4]** , **Scott England[5]** , **J. Scott Evans[4]** , **Matt Fillingim[6]**, **Rob Lillis[6]**, **Fatma Lootah[7]**, **Susarla Raghuram[1,3]**, **Frank Eparvier[1]**, **Ed Thiemann[1]**, **Shannon Curry[6]**, and **Hessa AlMatroushi[7]**

[1]LASP, University of Colorado at Boulder, Boulder, CO, USA, [2]UAE Space Agency, Abu Dhabi, United Arab Emirates, [3]Space and Planetary Science Center, Khalifa University, Abu Dhabi, United Arab Emirates, [4]Computational Physics Inc, Springfield, VA, USA, [5]Aerospace and Ocean Engineering, Virginia Polytechnic Institute and State University, Blacksburg, VA, USA, [6]Space Sciences Laboratory, University of California Berkeley, Berkeley, CA, USA, [7]Mohammed Bin Rashid Space Center, Al Khawaneej, United Arab Emirates

Abstract Water is lost from the Mars upper atmosphere to space as hydrogen and oxygen, both of which can be observed in scattered ultraviolet sunlight at 102.6 nm. We present Emirates Mars Mission Emirates Mars Ultraviolet Spectrometer (EMM/EMUS) insertion orbit observations of this airglow, resolving the independent altitude contributions of H and O for the first time. We present the first airglow modeling of the complete H and O 102.6 nm system and the first 3D azimuthally symmetric modeling of the O emission, retrieving temperatures and densities typical of northern spring. Our model reproduces the emission well above 200 km, but does not incorporate partial frequency redistribution needed to reproduce the observed O brightness at lower altitudes and on the disk. These results support future EMM/EMUS science orbit retrievals of H loss and the use of 102.6 nm observations to constrain planetary atmospheres across the solar system.

Plain Language Summary The Emirates Mars Ultraviolet Spectrometer (EMUS) on the Emirates Mars Mission (EMM) is the first Mars-orbiting instrument capable of observing extreme ultraviolet airglow, including light at 102.6 nm. Sunlight at this wavelength is scattered by both hydrogen and oxygen in the Mars upper atmosphere. Here we present the first observations capable of detecting the independent contributions of H and O to the emission brightness as a function of altitude. O contributes brightness close to the planet, because it is more massive and therefore more tightly confined by gravity than H. Our model can reproduce the shape of the observations above 200 km altitude, and determine that the atmosphere conditions are typical for the time period observed. At lower altitudes, the model prediction is dimmer than reality because the model does not include one of the ways that O atoms scatter sunlight when the atmosphere gets dense. These results lay a foundation for EMM science orbit data analysis, which will help us understand how H and O are distributed around Mars, how much H is escaping from Mars to space today, and how the planet has evolved over the history of the solar system.

1. Motivation for 102.6 nm Measurements at Mars

Upper atmospheric hydrogen at Mars scatters sunlight in the Lyman series, enabling retrieval of the H abundance and escape rate to space (Anderson, 1974). Over Mars history, such escape has removed a large fraction of the planet's initial water inventory (see Jakosky (2021) and Cangi et al. (2020) and references therein). Prior remote sensing retrievals of Mars H escape have focused on the H Lyman alpha emission at 121.6 nm due to two factors: the line's brightness, which gives a high signal-to-noise ratio, and to the abundance of Lyman alpha measurements by Mars-orbiting spacecraft and Earth-orbiting telescopes (Anderson, 1974; Bhattacharyya et al., 2015; Chaffin et al., 2014; Chaufray et al., 2008; Clarke et al., 2014; Qin, 2021). However, the line's brightnesses comes at a cost: its large scattering cross section means photons scatter multiple times in the planetary corona before they are detected. This multiple scattering leads to a moderate optical depth ($\tau \sim 1 - 10$) and introduces degeneracies between temperature, density, and the instrument absolute calibration that have been explored in some previous analyses (Bhattacharyya et al., 2015; Chaffin et al., 2018; Chaufray et al., 2008).

The Lyman beta line at 102.6 nm provides another window into the H distribution around the planet, but observations of this line at Mars have been rare. Disk-integrated measurements were provided by the Earth-orbiting

Hopkins Ultraviolet Telescope (HUT) (Feldman et al., 2000) and Far Ultraviolet Spectroscopic Explorer (Krasnopolsky & Feldman, 2002), with more recent Hisaki measurements giving spatial resolution comparable to the size of the disk (Masunaga et al., 2020). The only spacecraft flyby observation was made by Rosetta/Alice (Feldman et al., 2011), and only the optically thin H coronal 102.6 nm emission far from the disk was analyzed. The oscillator strength of Lyman beta is 0.079, versus the Lyman alpha value of 0.416, making Lyman beta about five times optically thinner than Lyman alpha. This places Lyman beta observations closer to the optically thin limit in which line brightness is directly proportional to the line of sight column density, permitting (in principle) an easier retrieval of density from observed brightness.

Despite its advantage in optical depth, Lyman beta airglow analysis is not without complications. The lower optical depth is bought at the price of signal-to-noise; in addition to the smaller cross section of the line, the Sun is fainter at Lyman beta than Lyman alpha by a factor of ~66 (Lemaire et al., 2012). In addition, the Lyman beta line falls extremely close to an optically thick neutral oxygen multiplet which overlaps the solar Lyman beta line, greatly complicating data analysis. Study of the combined H+O 102.6 nm system has so far been limited to the Earth atmosphere, using sounding rocket (Cotton et al., 1993; Meier et al., 1987) and HUT observations (Bishop & Feldman, 2003) employing plane-parallel radiative transfer modeling to track both the Lyman beta and O 102.6 nm emissions separately, with no previous modeling study able to completely match the observed intensities. Venus 102.6 nm data gathered during the Cassini flyby has never been fully analyzed because of the modeling difficulties encountered in the Earth atmosphere (Gérard et al., 2011). Here we present a new data set for 102.6 nm emission at Mars and a new analysis of the combined system using a 3D radiative transfer model.

2. EMM/EMUS Insertion Orbit Limb Scan Design and Data Analysis

The Emirates Mars Ultraviolet Spectrometer (EMUS) is a far-ultraviolet spectrograph designed for remote sensing of the upper atmosphere and corona (Holsclaw et al., 2021) as a part of the Emirates Mars Mission (EMM) (Almatroushi et al., 2021; Amiri et al., 2022). A key design requirement of this instrument was sensitivity to H Lyman beta in order to improve understanding of the optically thick H corona. Lyman beta defines the lower limit of the required wavelength range of 100–163 nm across the full airglow slit. EMUS was calibrated at 102.6 nm on the ground (Holsclaw et al., 2021), and flight comparisons of the brightness of Alpha Gru with SPICAV (Bertaux et al., 2007) spectra indicated that the instrument radiometric sensitivity below 125 nm was unchanged, with a slight sensitivity decrease relative to ground measurements noted at longer wavelengths. The spectral resolution of EMUS is variable due to a slit selection mechanism, and can be set to 0.4, 1.3, 1.8, or 5.0 nm, with the middle two options by far the most commonly used during normal science operations. During these operations EMUS makes images of the Mars disk and corona, and performs cross-orbit observations of the altitude profiles of H and O emissions to above 6 Mars radii. EMM's nominal science orbit is large, with a periapsis of ~20,000 km, so that even at its closest the 0.36° angular resolution of the instrument leads to a 125 km footprint on the planet.

A key goal of EMM/EMUS is to combine disk and corona observations of Lyman alpha and Lyman beta gathered at all phase angles to constrain the 3D structure of the H corona. Discriminating between the H and O contributions to 102.6 nm brightness on the disk is a necessary prerequisite to achieving this goal. At the spectral resolution of EMUS, the H and O 102.6 nm contributions can be distinguished using the gravity of Mars as a filter, either by observing at a sufficient pointing distance from the planet that the O contribution is negligible, or by resolving the transition in the emission scale height at the limb, where the O contribution falls off much more quickly than H due to the 16× mass difference between the species. Intuition about where the transition between the two contributions occurs can be gained by comparison with atomic O resonance scattering at 130.4 nm, which produces a visible thermal O corona out to about 500 km, beyond which hot O contributions dominate the brightness (Deighan et al., 2015). Hot O is about as gravitationally bound to the planet as thermal H, and the strongest line in the O 102.6 nm multiplet overlapping the solar line has an *f*-value of 0.016, near the *f*-values of 0.05 for O I 130.4 nm. Furthermore, the solar flux at 102.6 is comparable to that at 130.4, so that a limb profile of 102.6 emission can be expected to have a shape similar to 130.4 nm, with thermal O contributions falling off steeply below ~500 km superseded by thermal H contributions at higher altitudes. Unfortunately, as described above, in normal science operations the spatial resolution of EMUS is incapable of detecting this transition.

In order to obtain data capable of resolving O and H contributions to the 102.6 nm brightness and validate disk retrieval techniques for this and other emissions observed by EMUS, special observations were designed for the
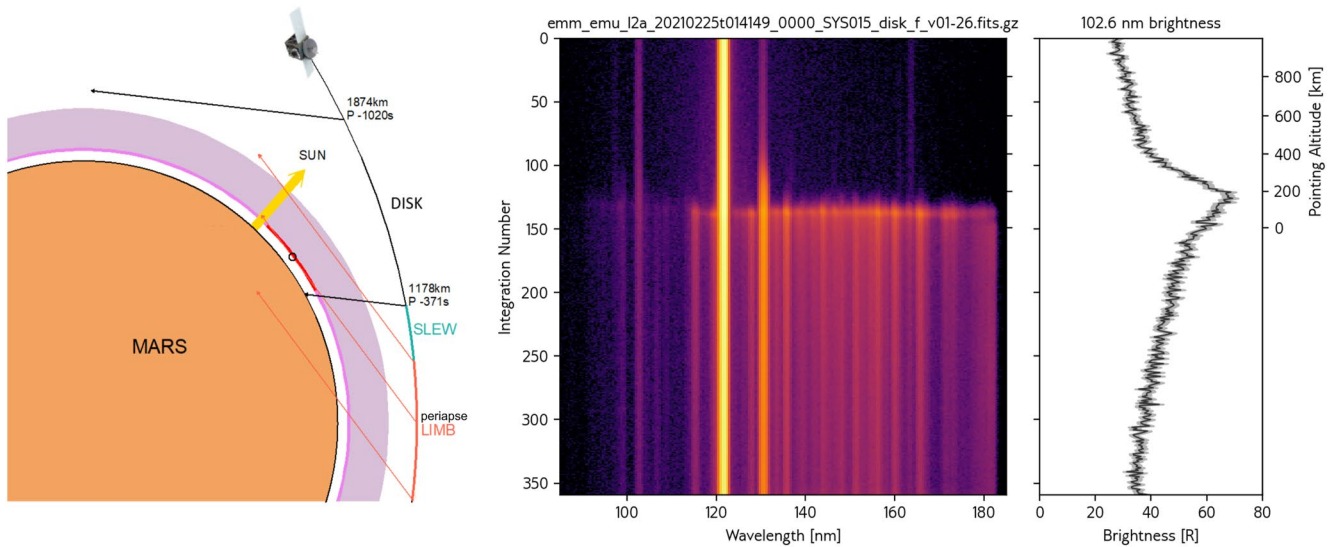
Figure 1. Observation design and data for Emirates Mars Mission (EMM) insertion orbit limb scans. (left) EMM spacecraft insertion orbit and observation geometry. Vectors indicate the look direction of the instrument, which is reoriented between the "DISK" (black) and "LIMB" (red) observations. Here we use only the "DISK" data set, which extends to higher altitudes. (center) Observed slit-averaged spectrum as a function of integration number and pointing altitude for the indicated disk observation. Color indicates log spectral radiance on a perceptual scale. Limb dayglow extends across most wavelengths at altitudes below 200 km. At higher altitudes the spectrum consists of coronal signatures from H and O, including H Lyman beta and O emission at 102.6 nm, and a Lyman alpha ghost image near 160 nm. (right) Observed limb profile of 102.6 nm emission coadded over all eight disk scans, showing a clear change in scale height near 400 km due to the transition from contributions dominated by O to those from H.

EMM insertion orbit, in which periapsis was still low enough to permit atmospheric limb scans. A schematic diagram of these observations is given in Figure 1 (left). Two observation sequences were designed, the first before periapsis, measuring tangent point altitudes below ~1,000 km and extending onto the disk near the tangent point of a second set of limb observations gathered around periapsis. These observations were repeated on eight orbits spanning 25 February 2021–9 March 2021 ($L_s \sim 10°$), with four orbits using the 0.4 nm slit and the remainder using the 1.3 nm slit.

Figure 1 (center) presents an altitude spectrum gathered by EMUS with the 1.3 nm slit during the pre-periapse "DISK" scan. Because these "DISK" scans extend to higher altitudes more sensitive to H 102.6 nm emission contributions, we use only these in our subsequent analysis. We integrated the spectrum from 101 to 104 nm to obtain the 102.6 nm brightness for each observation, then coadded all observations integration-by-integration with weights equal to the square root of the number of counts observed in each observation/integration. Assuming poisson-distributed counts, this coaddition provides the best estimate of the true count rate/brightness seen in each integration. The resulting coadded profile is shown as a black curve in the right panel of Figure 1, with gray contours representing the derived standard deviation of the mean. The slope change from contributions due to oxygen and hydrogen is clearly visible at an altitude of ~400 km, in line with the intuition developed above. Modest limb brightening is visible below 200 km, decreasing slowly to near-constant brightness values as the line of sight moves onto the disk. The average EMUS observed 102.6 nm brightness above the limb of ~30 R is comparable to that observed during the Rosetta flyby (Feldman et al., 2011) in the closest bin to the limb, whose size was about 1,000 km.

3. Model Description and Data Comparison

In order to retrieve the H and O density and temperature from these observations, we employ a 3D radiative transfer model. The model is descended from earlier models used for optically thick coronal studies, including those of Anderson and Hord (1977), Bishop (1999), and Chaffin et al. (2018), but was completely redesigned and reimplemented for this work. A complete description of the model and its full capabilities will be given in a later paper; we sketch the salient details here and provide all model code at the link given in the open research statement should anyone wish to examine details we do not discuss, or reproduce our results.

The model is a 3D finite-element code following the geometric implementation of Anderson and Hord (1977), which divides the region around Mars into voxels on a polar grid in solar zenith angle and radius, and assumes symmetry about the Mars-Sun axis. We assume atmosphere and radiation field properties are constant inside each voxel, and include multiple scattering effects via line-of-sight integrations through the atmosphere that estimate photon scattering between the voxels. These integrals incorporate both pure absorption due to CO_2 and absorption into the upper state of the radiatively active atoms on a wavelength grid with a spacing of 0.4 Doppler widths, subsampling each modeled spectral line. We model H Lyman beta as a singlet assuming complete frequency redistribution and isotropic emission, as has been common in modeling of the H Lyman alpha emissions at Mars (Anderson, 1974; Bhattacharyya et al., 2015; Chaffin et al., 2014; Chaufray et al., 2008; Clarke et al., 2014). We further assume a temperature-dependent Doppler line shape based on the local atmospheric temperature, which along with the other assumptions allows us to track only the density of upper states in each voxel rather than more detailed information about the radiation field. The single-scattering excited state density in each voxel is computed as the product of the optically thin density and atmospheric extinction. For H Lyman beta, we compute the optically thin density as $n_u = \pi F_\odot \sigma_{lu} n_l / \Sigma A_{uL}$, where n_u [cm^{-3}] is the upper state density, $\pi F_\odot$ [ph cm^{-2} s^{-1} Hz^{-1}] is the Lyman beta line center solar flux, σ_{lu} [cm^2 Hz] is the total cross section of the Lyman beta line, n_l [cm^{-3}] is the density of the lower state (effectively the total H number density), and ΣA_{uL} [s^{-1}] is the sum of the Einstein A values connecting the Lyman beta upper state to all possible lower states (i.e., both Lyman beta and Balmer alpha).

For O 102.6 nm emission, six lines couple three upper and lower states, as shown in Figure 2 (left). Lines with lower level $J = 2$ overlap the solar Lyman beta line and pump the multiplet system, with contributions from the other lower states assumed negligible. We use line data from Wiese et al. (1996), as compared with Meier et al. (1987), who used slightly different line values from Pradhan and Saraph (1977). Exactly as for H, we assume temperature-dependent Doppler line shapes, complete frequency redistribution, and isotropic emission. Because of the high optical depth of O 102.6 nm at Mars, assuming complete frequency redistribution is suspect at low altitudes; we discuss this more completely below. For O, independent tracking of all three upper states and the radiative interaction of the lines significantly complicates the model, to the extent that all earlier airglow studies of this emission used a singlet approximation instead. Here, we track each state and multiplet separately, including branching to the 1,129 nm multiplet, resulting in both the first complete description of this atomic line system in an airglow context and the first 3D (azimuthally symmetric) model of this O emission in the planetary literature. To accomplish this, we use the same scattering code as for H, but track emission/absorption via each line in each voxel to compute the scattering from the upper states of each voxel to all other voxel upper states. Not all of the O lines are close enough to radiatively interact; we track the singlet, doublet, and triplet components on independent wavelength grids. We do not consider radiative interaction of planetary H Lyman beta and O emissions, because the shortest line in the O system and H Lyman beta are separated by about six H Lyman beta Doppler widths at 200 K. For single scattering calculations, we populate the O ground state energy levels using a Boltzmann/Gibbs distribution appropriate to the local voxel temperature, and compute the optically thin density using the same expression as for Lyman beta, substituting the relevant values for the O atom and using the $J = 2$ lower state density for n_l as this state is the only one whose lines overlap solar Lyman beta.

We assume a physical atmosphere density and temperature distribution identical to that used in prior modeling (Chaffin et al., 2014, 2018; Chaufray et al., 2008), and consider three input variables: the 200 km exobase temperature and the density of H and O at this altitude. The temperature structure of the atmosphere below the exobase is specified analytically as in Krasnopolsky (2002), with CO_2 below the exobase defined hydrostatically and H/O densities computed using the diffusion equation as in Chaufray et al. (2008) with the appropriate H/O diffusion coefficients. We use a fixed CO_2 exobase density of 1.0×10^7 cm^{-3}, a typical value for $L_s \sim 0°$ based on the Mars Climate Database (Millour et al., 2015). Above the exobase, we assume the atmosphere is isothermal at the exobase temperature, and that species densities follow spherically symmetric Chamberlain exosphere distributions (Chamberlain, 1963). For the input solar brightness, we interpolate the measured broadband solar Lyman alpha brightness from MAVEN's Extreme UltraViolet Monitor (EUVM) (Eparvier et al., 2015) to the time of the EMUS observation, and convert to line-center brightness using the relationship of Emerich et al. (2005). To convert this to solar Lyman beta line center brightness we divide by 66, the value used by Meier et al. (1987), which is within the uncertainty envelope of the expected value based on the solar line ratio study of Lemaire et al. (2012) and the observed EUVM solar brightness, obtaining a g-value at Mars of 2.05×10^{-6} s^{-1}. We assume all solar lines are flat across the width of the planetary lines, and that there is no significant 102.6 nm
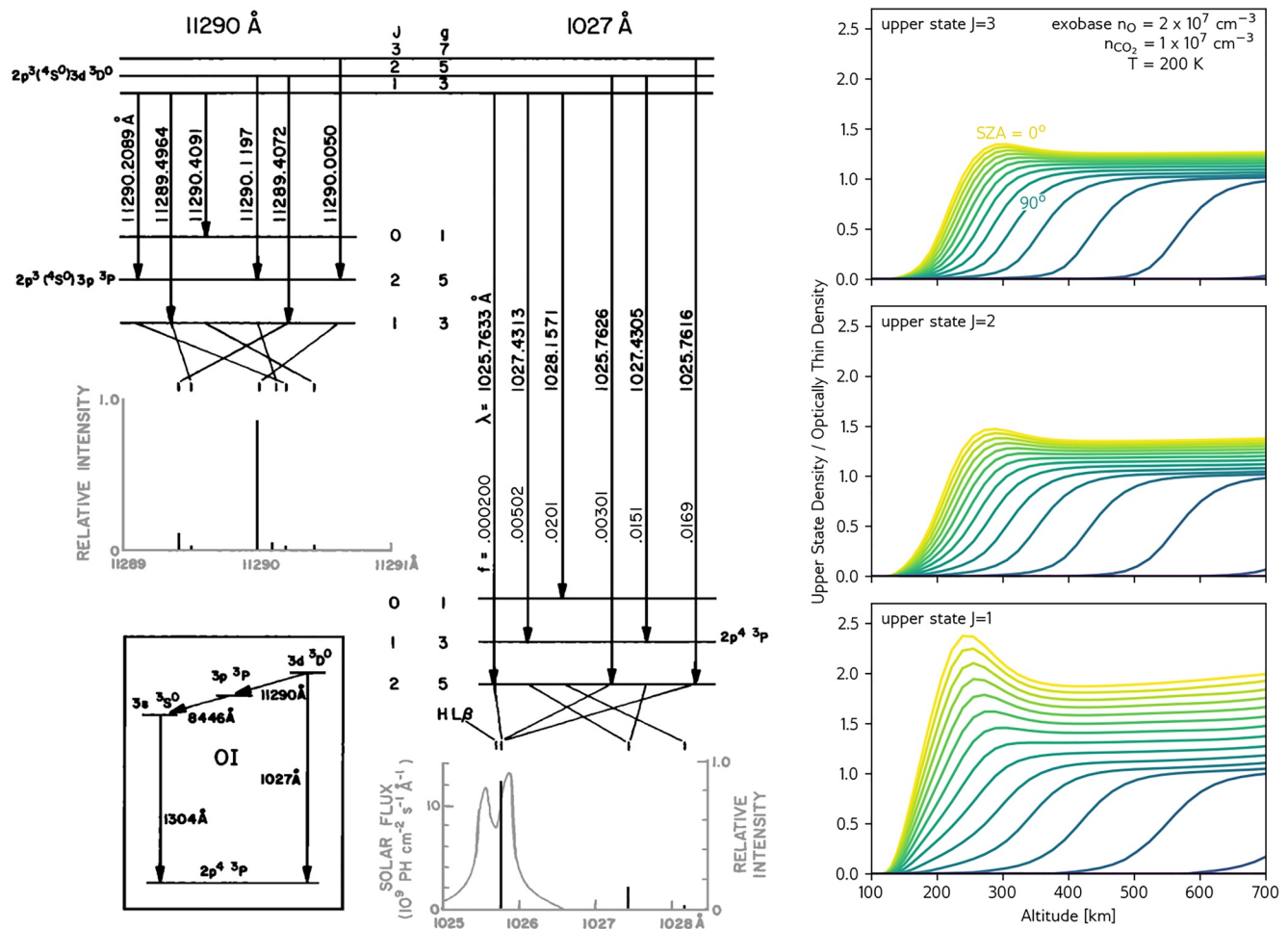
Figure 2. O 102.6 nm energy level diagram adapted from Meier et al. (1987) and our computed model O upper state densities. (left) Partial diagram of O electronic states, including the ground $2p^4\ ^3P$ state, the $2p^3\ 3d\ ^3D^0$ state resulting from absorption of solar Lyman beta sunlight, and the $2p^3\ 3p\ ^3P$ state to which this upper state can flouresce via 1.129 μ m emission. Wavelengths, *f*-values, and relative line strengths used here are indicated as appropriate. (right) Our model predictions of the upper state density of each level relative to what would be produced via optically thin scattering (see text). These calculations were performed for the best-fit exobase O density and temperature shown at upper right. Each panel shows the upper state density as a function of altitude and solar zenith angle. These results represent the first calculation of all O 102.6 nm upper state densities and the first 3D azimuthally symmetric calculation for any of the upper states.

interplanetary background. While the O 102.6 nm triplet is displaced from line center and should therefore see a slightly higher solar brightness than H (as shown in Figure 2, left), we used the same solar brightness for both species.

Our model results for Lyman beta are a straightforward extension of earlier results for Lyman alpha that have been extensively described elsewhere (Anderson & Hord, 1977; Bhattacharyya et al., 2015; Bishop, 1999; Chaffin et al., 2018; Chaufray et al., 2008); we do not repeat this description here. Figure 2 (right) shows our modeled O upper state density for best-fit parameters to the observed 102.6 nm emission given below. Because of the strength of the $J = 3 \rightarrow 2$ line, upper state densities are dominated by the $J = 3$ state, accounting for approximately 80% of the total, slightly lower than the expected 84% partitioning based on *f*-values. The vast majority of the remaining 20% of upper state densities is accounted for by the $J = 2$ state. Because the $J = 1$ state has the weakest solar pumping of the three upper states, its density is the most enhanced relative to optically thin conditions due to redistribution by fluorescent scattering from the other upper states. We find that the overall $J = 3$ upper state density is enhanced by 30%–40% relative to optically thin conditions by multiple scattering. Compared to the single scattering density, which is the optically thin density times the extinction due to atmospheric absorption, the upper state densities are larger by a factor of ~3.5, in agreement with the branching ratio to the 1,129 nm line of ~0.29 and the escape probability argument given by Meier et al. (1987). At the highest altitudes in the model,
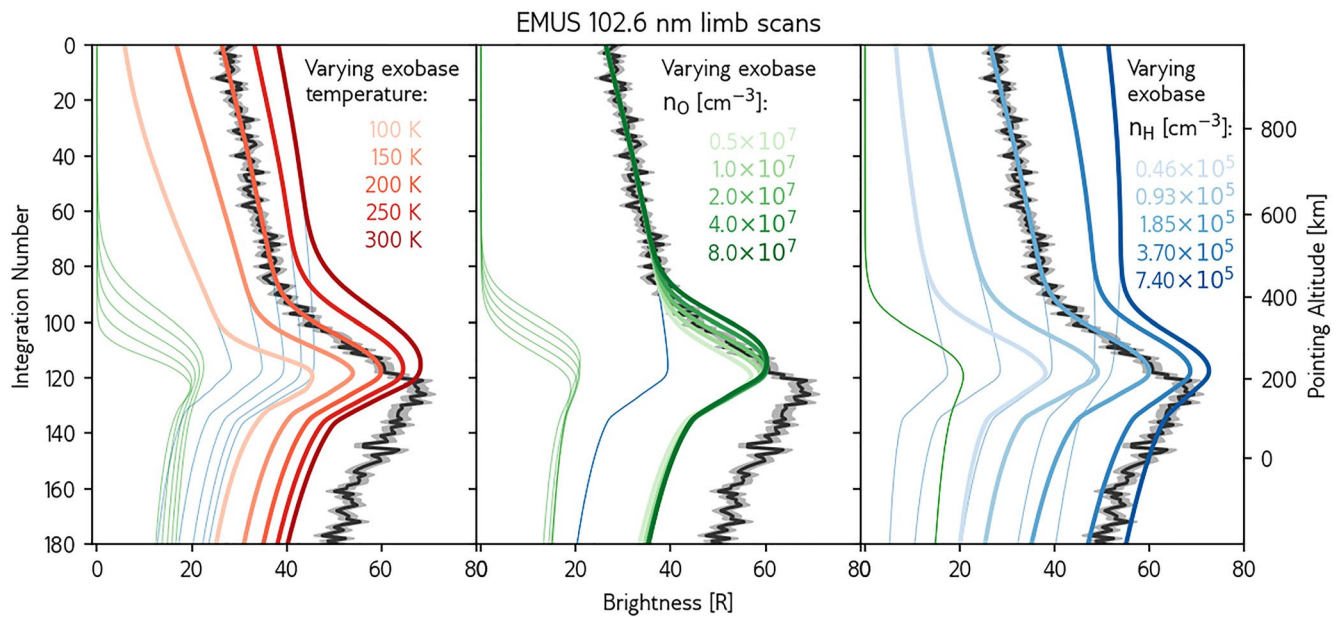
Figure 3. Coadded EMUS 102.6 nm limb scan profile with best-fit model profile and sensitivity study. In each panel, the black and gray curves show the EMUS-observed 102.6 nm brightness shown in Figure 1 (right). Thin blue and green curves show modeled contributions of H and O, which sum to the thick curves representing total emission brightness. Each panel shows the effect of varying one of the model fit parameters. (left) Variations in exobase temperature alter the scale height of the O contribution, with a modest effect on the H scale height. Both H and O brightness increase with temperature because the species velocity distribution gets wider and scatters more photons from the solar line. (center) Varying the O exobase density mainly increases the altitude of the O emission contributions, as expected based on the high optical depth of the line. (right) Variations in H density produce the largest changes in brightness and profile topside slope, indicating a well-known degeneracy in density and temperature for optically thick H lines. No model matches the observed disk brightness (see discussion in text), but the match above 200 km is good, indicating that the model can retrieve species densities and temperature from brightness.

our predicted upper state densities are higher than the optically thin expectation due to Mars-shine illumination from below, producing a ~20% enhancement in brightness near the subsolar point.

To avoid a model/data mismatch at low altitudes discussed more completely below from confusing an automated fitting routine, we determine best-fit parameters by eye for the exobase temperature and O/H densities. The best-fit brightness resulting from the combined H and O model and a set of sensitivity studies around this best-fit are shown in Figure 3. The model correctly reproduces the scale height transition near 400 km for an exobase temperature of 200 K, H exobase density of 1.85×10^5 cm^{-3} and O exobase density of 2×10^7 cm^{-3}, values that are not surprising for Mars northern spring equinox conditions based on the Mars Climate Database (Millour et al., 2015). These values are in family with prior results available for the same season, including: Stone et al. (2022), who found $n_O \sim 2 \times 10^7$ cm^{-3} at our exobase $n_{CO_2} = 1.0 \times 10^7$ cm^{-3}; Chaffin et al. (2014) who found for their orbit 5,070 that an assumed exobase temperature of 180 K gave $n_H = 1.4 \times 10^5$ cm^{-3}; Halekas (2017), who found $n_H \sim 3 \times 10^5$ cm^{-3} for an assumed exobase temperature of 200 K; and Qin (2021), who found temperatures near 200 K and H densities near 8×10^4 cm^{-3}. Other recent studies of H and O in the thermosphere either did not report retrievals or had no data covering northern spring equinox (Bhattacharyya et al., 2015; Chaffin et al., 2018; Chaufray et al., 2008, 2015; Feldman et al., 2011; Masunaga et al., 2020; Qin, 2020). Importantly, we require no modification to the instrument calibration or solar flux to obtain a good model/data match. A full retrieval incorporating a nuisance parameter for the instrument calibration/solar flux could potentially improve the data-model match and understanding of parameter degeneracies, but we defer this analysis to a future paper describing the EMM/EMUS disk H analysis pipeline.

Sensitivity studies reveal the importance of each parameter in determining a good match to the data. Changes in atmospheric temperature mostly lead to changes in emission brightness due to the broader Doppler width of the planetary line, which captures and scatters more solar photons. Variations in the O density mostly shift the best-fit model profile up and down in altitude, with only a secondary effect on line brightness, as is expected for the optically thick O line. Note that brightness on the disk (integrations 140+) is nearly constant with increasing O density above the best fit, indicating the Doppler line we model has nearly exhausted its ability to scatter solar

photons. Variations in H density lead mostly to changes in emission brightness, with larger changes in the slope of the emission profile at coronal altitudes >500 km than for temperature, revealing once again a known degeneracy in temperature and density for optically thick H emissions (Bhattacharyya et al., 2017; Chaffin et al., 2014; Chaufray et al., 2008), though with more modest effects in the present analysis than for the thicker H 121.6 nm line.

No model fits the brightness at 102.6 nm below ∼200 km or on the disk, and the sensitivity study indicates that variations in the selected parameters cannot produce a match. The discrepancy is likely due to the model assumption of complete frequency redistribution with a Doppler line profile, which severely limits the ability of low-altitude oxygen to intercept and scatter sunlight in the wings of the line system. In the best fit atmosphere the $\tau = 1$ level for 102.6 nm CO_2 absorption is at 130 km, by which point the thickest line of the O system has a vertical optical depth of ∼30, large enough that the natural line wings can begin to scatter sunlight far from the core velocity distribution of O atoms in the atmosphere. Photons scattered at these distant wavelengths retain their separation from the core because each scattering provides only a relatively small Doppler shift consistent with the O atom velocity distribution. As a result, these distant wing photons typically scatter only once or twice in the atmosphere, providing a boost in brightness at lower altitudes where the core of the line is completely extincted. Including this partial frequency distribution process in the model is possible (Bush & Chakrabarti, 1995), but beyond the scope of the current analysis, which demonstrates that the 102.6 nm emission brightness can be reproduced at altitudes greater than ∼200 km assuming complete frequency redistribution. Because the Doppler core and line wings are largely separate in their contributions to the emission, we do not expect future modeling incorporating the wing contributions to produce a large difference in derived best-fit parameters.

Another possibility to increase the modeled 102.6 nm brightness at low altitudes discussed in previous Earth studies of 102.6 nm emission is electron impact excitation of atomic oxygen. Cotton et al. (1993) and Bishop and Feldman (2003) both considered this potential source, which dominates the volume emission rate at low altitudes in their Earth models. Somewhat surprisingly, however, the effect of electron impact on the modeled brightness in these studies was negligible, because photons created by this process are produced in the Doppler core of the line and are trapped in the optically thick region of the atmosphere until they branch to the 1,129 nm line after several scatterings. Similar arguments apply to any brightness changes produced by local variability in atmospheric oxygen density in the lower thermosphere. Nevertheless, a possibility for topside electron impact excitation exists, which should be investigated in future studies that more completely model this line system at Mars.

4. Prospects for Disk and Corona Observations of Mars 102.6 nm Emission

We have presented the first study of the independent contributions of H and O to 102.6 nm emission at Mars, using altitude-resolved measurements to separate the species via their scale height difference. In addition, we present the first complete model of the 102.6 nm oxygen sextuplet incorporating all lines and levels in an airglow context, and the first model of any line or level of this system in more than 1D. We demonstrate that a model exobase temperature of 200 K, H density of 1.85×10^5 cm^{-3}, and O density of 2×10^7 cm^{-3}, in line with prior observations and modeling of northern spring equinox, can reproduce the observed shape and magnitude of the emission above ∼200 km, without modification to the instrument absolute calibration or solar flux. Finally, we show that our assumption of complete frequency redistribution is insufficient to correctly reproduce the O 102.6 nm brightness below ∼300 km and on the disk, suggesting that partial frequency redistribution will be needed to reproduce the full brightness profile.

This work has been partly in preparation for EMM/EMUS science mission data analysis, which produces weekly observations of the H corona from all phase angles at wavelengths of 102.6 and 121.6 nm. Analysis of this data set will require a model that can reproduce the disk 102.6 nm brightness simultaneously with the 121.6 nm brightness, or require masking the disk out when performing coronal retrievals. Data and models from Figure 3 show that O contributions above 500 km are very small, so that a mask removing data below this altitude could permit 102.6 nm modeling neglecting O contributions to successfully reproduce coronal observations. Inclusion of the observed disk brightness in fitting such models would still be possible via 121.6 nm H Lyman alpha, but this would likely be complicated by the presence of deuterium (Chaufray et al., 2021) and/or proton aurora (Hughes et al., 2019).

Beyond H coronal analysis from the Emirates Mars science mission, the present work has implications for understanding the physics of O and H emissions at Mars and other planets. Our analysis at Mars was able to reproduce the shape and magnitude of the coronal emission, unlike earlier analyses of 102.6 nm emission at Earth, opening the possibility for using O 102.6 nm observations to constrain the upper atmospheric abundance of H and O at Mars and other terrestrial planets. Additional modeling studies will be needed to assess seasonal and solar variability in both H and O emissions at 102.6 nm to achieve EMM's goal of retrieving the coronal H abundance in 3D and the escape rate of H from the planet. Known seasonal variability in H escape is likely to increase the proportion of 102.6 nm brightness due to H in Southern Summer while decreasing that of O, but the combined effect on the 102.6 nm airglow has never been predicted or observed. Such an assessment will be needed to fold these measurements into the overall story of H loss at Mars and determine their implications for the long term evolution of the planet.

Data Availability Statement

The EMM/EMUS l2a SYS.015 data we analyze here are available at the EMM Science Data Center (SDC, http://sdc.emiratesmarsmission.ae). This location is designated as the primary repository for all data products produced by the EMM team and is designated as long-term repository as required by the UAE Space Agency. The data available (http://sdc.emiratesmarsmission.ae/data) include ancillary spacecraft data, instrument telemetry, Level 1 (raw instrument data) to Level 3 (derived science products), quicklook products, and data users guides (https://sdc.emiratesmarsmission.ae/documentation) to assist in the analysis of the data. Following the creation of a free login, all EMM data are searchable via parameters such as product file name, solar longitude, acquisition time, sub-spacecraft latitude and longitude, instrument, data product level, and etc. Data products can be browsed within the SDC via a standardized file system structure that follows the convention:`/emm/data/<Instrument>/<DataLevel>/<Mode>/<Year>/<Month>` Data product filenames follow a standard convention: `emm_<Instrument>_<DataLevel>_<StartTimeUTC>_<OrbitNumber>_<Mode>_<Description>_<KernelLevel>_<Version>.<FileType>` Emirates Mars Ultraviolet Spectrometer (EMUS) data and users guides are available at: https://sdc.emiratesmarsmission.ae/data/emus. MAVEN EUVM l2 data used to infer the solar Lyman alpha and Lyman beta brightness at Mars is available at the Plantary Data System Planetary Plasma Interactions Node, https://pds-ppi.igpp.ucla.edu/search/view/?id=pds://PPI/maven.euv.calibrated. The coronal airglow model used to reproduce the 102.6 nm brightness is archived on Zenodo, https://doi.org/10.5281/zenodo.6930426.

References

Almatroushi, H., AlMazmi, H., AlMheiri, N., AlShamsi, M., AlTunaiji, E., Badri, K., et al. (2021). Emirates Mars mission characterization of Mars atmosphere dynamics and processes. *Space Science Reviews*, *217*(8), 89. https://doi.org/10.1007/s11214-021-00851-6

Amiri, H. E. S., Brain, D., Sharaf, O., Withnell, P., McGrath, M., Alloghani, M., et al. (2022). The emirates Mars mission. *Space Science Reviews*, *218*(1), 4. https://doi.org/10.1007/s11214-021-00868-x

Anderson, D. E., & Hord, C. W. (1977). Multidimensional radiative transfer: Applications to planetary coronae. *Planetary and Space Science*, *25*(6), 563–571. https://doi.org/10.1016/0032-0633(77)90063-0

Anderson, D. E., Jr. (1974). Mariner 6, 7, and 9 ultraviolet spectrometer experiment: Analysis of hydrogen Lyman alpha data. *Journal of Geophysical Research*, *79*(10), 1513–1518. https://doi.org/10.1029/JA079i010p01513

Bertaux, J.-L., Nevejans, D., Korablev, O., Villard, E., Quémerais, E., Neefs, E., et al. (2007). SPICAV on Venus express: Three spectrometers to study the global structure and composition of the Venus atmosphere. *Planetary and Space Science*, *55*(12), 1673–1700. https://doi.org/10.1016/j.pss.2007.01.016

Bhattacharyya, D., Clarke, J., Bertaux, J.-L., Chaufray, J.-Y., & Mayyasi, M. (2017). Analysis and modeling of remote observations of the Martian hydrogen exosphere. *Icarus*, *281*, 264–280. https://doi.org/10.1016/j.icarus.2016.08.034

Bhattacharyya, D., Clarke, J. T., Bertaux, J.-L., Chaufray, J.-Y., & Mayyasi, M. (2015). A strong seasonal dependence in the Martian hydrogen exosphere. *Geophysical Research Letters*, *42*(20), 8678–8685. https://doi.org/10.1002/2015gl065804

Bishop, J. (1999). Transport of resonant atomic hydrogen emissions in the thermosphere and geocorona: Model description and applications. *Journal of Quantitative Spectroscopy and Radiative Transfer*, *61*(4), 473–491. https://doi.org/10.1016/s0022-4073(98)00031-4

Bishop, J., & Feldman, P. D. (2003). Analysis of the Astro-1/Hopkins ultraviolet telescope EUV-FUV dayside nadir spectral radiance measurements. *Journal of Geophysical Research*, *108*, 1243. https://doi.org/10.1029/2001ja000330

Bush, B. C., & Chakrabarti, S. (1995). A radiative transfer model using spherical geometry and partial frequency redistribution. *Journal of Geophysical Research*, *100*(A10), 19627–19642. https://doi.org/10.1029/95JA01209

Cangi, E. M., Chaffin, M. S., & Deighan, J. (2020). Higher Martian atmospheric temperatures at all altitudes increase the D/H fractionation factor and water loss. *Journal of Geophysical Research: Planets*, *125*, e06626. https://doi.org/10.1029/2020je006626

Chaffin, M. S., Chaufray, J. Y., Deighan, J., Schneider, N. M., Mayyasi, M., Clarke, J. T., et al. (2018). Mars H escape rates derived from MAVEN/IUVS Lyman alpha brightness measurements and their dependence on model assumptions. *Journal of Geophysical Research: Planets*, *123*, 2192–2210. https://doi.org/10.1029/2018je005574

Chaffin, M. S., Chaufray, J.-Y., Stewart, I., Montmessin, F., Schneider, N. M., & Bertaux, J.-L. (2014). Unexpected variability of Martian hydrogen escape. *Geophysical Research Letters*, *41*(2), 314–320. https://doi.org/10.1002/2013gl058578

Chamberlain, J. W. (1963). Planetary coronae and atmospheric evaporation. *Planetary and Space Science*, *11*(8), 901–960. https://doi.org/10.1016/0032-0633(63)90122-3

Chaufray, J. Y., Bertaux, J. L., Leblanc, F., & Quémerais, E. (2008). Observation of the hydrogen corona with SPICAM on Mars express. *Icarus*, *195*(2), 598–613. https://doi.org/10.1016/j.Icarus.2008.01.009

Chaufray, J. Y., Deighan, J., Chaffin, M. S., Schneider, N. M., McClintock, W. E., Stewart, A. I. F., et al. (2015). Study of the Martian cold oxygen corona from the OI 130.4 nm by IUVS/MAVEN. *Geophysical Research Letters*, *42*(21), 9031–9039. https://doi.org/10.1002/2015gl065341

Chaufray, J. Y., Mayyasi, M., Chaffin, M., Deighan, J., Bhattacharyya, D., Clarke, J., et al. (2021). Estimate of the D/H ratio in the Martian upper atmosphere from the low spectral resolution mode of MAVEN/IUVS. *Journal of Geophysical Research: Planets*, *126*, e06814. https://doi.org/10.1029/2020je006814

Clarke, J. T., Bertaux, J.-L., Chaufray, J.-Y., Gladstone, G. R., Quemerais, E., Wilson, J. K., & Bhattacharyya, D. (2014). A rapid decrease of the hydrogen corona of Mars. *Geophysical Research Letters*, *41*(22), 8013–8020. https://doi.org/10.1002/2014GL061803

Cotton, D. M., Chakrabarti, S., & Gladstone, G. R. (1993). Preliminary results from the berkeley EUV airglow rocket spectrometer: OI and N$_2$ FUV/EUV dayglow in the thermosphere and lower exosphere. *Journal of Geophysical Research*, *98*(A12), 21627–21642. https://doi.org/10.1029/93ja02267

Deighan, J., Chaffin, M. S., Chaufray, J.-Y., Stewart, A. I. F., Schneider, N. M., Jain, S. K., et al. (2015). MAVEN IUVS observation of the hot oxygen corona at Mars. *Geophysical Research Letters*, *42*(21), 9009–9014. https://doi.org/10.1002/2015GL065487

Emerich, C., Lemaire, P., Vial, J.-C., Curdt, W., Schühle, U., & Wilhelm, K. (2005). A new relation between the central spectral solar HI Lyman α irradiance and the line irradiance measured by SUMER/SOHO during the cycle 23. *Icarus*, *178*(2), 429–433. https://doi.org/10.1016/j.Icarus.2005.05.002

Eparvier, F. G., Chamberlin, P. C., Woods, T. N., & Thiemann, E. M. B. (2015). The solar extreme ultraviolet monitor for MAVEN. *Space Science Reviews*, *195*(1–4), 293–301. https://doi.org/10.1007/s11214-015-0195-2

Feldman, P. D., Burgh, E. B., Durrance, S. T., & Davidsen, A. F. (2000). Far-ultraviolet spectroscopy of Venus and Mars at 4 Å resolution with the Hopkins ultraviolet telescope on astro-2. *Acta Pathologica Japonica*, *538*(1), 395–400. https://doi.org/10.1086/309125

Feldman, P. D., Steffl, A. J., Parker, J. W., A'Hearn, M., Bertaux, J.-L., Alan Stern, S., et al. (2011). Rosetta -Alice observations of exospheric hydrogen and oxygen on Mars. *Icarus*, *214*(2), 394–399. https://doi.org/10.1016/j.Icarus.2011.06.013

Gérard, J. C., Hubert, B., Gustin, J., Shematovich, V. I., Bisikalo, D., Gladstone, G. R., & Esposito, L. W. (2011). EUV spectroscopy of the Venus dayglow with UVIS on Cassini. *Icarus*, *211*(1), 70–80. https://doi.org/10.1016/j.icarus.2010.09.020

Halekas, J. S. (2017). Seasonal variability of the hydrogen exosphere of Mars. *Journal of Geophysical Research: Planets*, *122*, 901–911. https://doi.org/10.1002/2017JE005306

Holsclaw, G. M., Deighan, J., Almatroushi, H., Chaffin, M., Correira, J., Evans, J. S., et al. (2021). The emirates Mars ultraviolet spectrometer (EMUS) for the EMM mission. *Space Science Reviews*, *217*(8), 79. https://doi.org/10.1007/s11214-021-00854-3

Hughes, A., Chaffin, M., Mierkiewicz, E., Deighan, J., Jain, S., Schneider, N., et al. (2019). Proton aurora on Mars: A dayside phenomenon pervasive in southern summer. *Journal of Geophysical Research: Space Physics*, *124*, 10533–10548. https://doi.org/10.1029/2019ja027140

Jakosky, B. M. (2021). Atmospheric loss to space and the history of water on Mars. *Annual Review of Earth and Planetary Sciences*, *49*(1), 71–93. https://doi.org/10.1146/annurev-earth-062420-052845

Krasnopolsky, V. A. (2002). Mars' upper atmosphere and ionosphere at low, medium, and high solar activities: Implications for evolution of water. *Journal of Geophysical Research*, *107*, 5128. https://doi.org/10.1029/2001JE001809

Krasnopolsky, V. A., & Feldman, P. D. (2002). Far ultraviolet spectrum of Mars. *Icarus*, *160*(1), 86–94. https://doi.org/10.1006/icar.2002.6949

Lemaire, P., Vial, J. C., Curdt, W., Schühle, U., & Woods, T. N. (2012). The solar hydrogen Lyman α to Lyman β line ratio. *Astronomy & Astrophysics*, *542*, L25. https://doi.org/10.1051/0004-6361/201219026

Masunaga, K., Yoshioka, K., Chaffin, M. S., Deighan, J., Jain, S. K., Schneider, N. M., et al. (2020). Martian oxygen and hydrogen upper atmospheres responding to solar and dust storm drivers: Hisaki space telescope observations. *Journal of Geophysical Research: Planets*, *125*, e06500. https://doi.org/10.1029/2020je006500

Meier, R. R., Anderson, D. E., Jr., Paxton, L. J., McCoy, R. P., & Chakrabarti, S. (1987). The OI 3d 3d°-2p43p transition at 1026 Å in the day airglow. *Journal of Geophysical Research*, *92*(A8), 8767–8774. https://doi.org/10.1029/ja092ia08p08767

Millour, E., Forget, F., Spiga, A., Navarro, T., Madeleine, J.-B., Montabone, L., et al. (2015). The Mars climate database (mcd version 5.2). *European Planetary Science Congress*, *10*, EPSC2015–438. held 27 September - 2 October, 2015 in Nantes, France.

Pradhan, A. K., & Saraph, H. E. (1977). Oscillator strengths for dipole transitions in neutral oxygen. *Journal of Physics B: Atomic and Molecular Physics*, *10*(17), 3365–3376. https://doi.org/10.1088/0022-3700/10/17/010

Qin, J. (2020). Mars upper atmospheric temperature and atomic oxygen density derived from the OI 130.4 nm emission observed by NASA's Maven mission. *The Astronomical Journal*, *159*(5), 206. https://doi.org/10.3847/1538-3881/ab7fae

Qin, J. (2021). Solar cycle, seasonal, and dust-storm-driven variations of the Mars upper atmospheric state and H escape rate derived from the lyα emission observed by NASA's MAVEN mission. *Acta Pathologica Japonica*, *912*(1), 77. https://doi.org/10.3847/1538-4357/abed4f

Stone, S. W., Yelle, R. V., Benna, M., Elrod, M. K., & Mahaffy, P. R. (2022). Neutral composition and horizontal variations of the Martian upper atmosphere from Maven NGIMS. *Journal of Geophysical Research: Planets*, *127*(6), e07085. https://doi.org/10.1029/2021je007085

Wiese, W. L., Fuhr, J. R., & Deters, T. M. (1996). Atomic transition probabilities of carbon, nitrogen, and oxygen: A critical data compilation.